Catalytic Activity of Pd-Doped UiO-66 MOF in Magnesium Hydrogenation/Dehydrogenation Process

R. K. Baimuratova[a], *, G. I. Dzhardimalieva[a, b], **, S. A. Mozhzhukhin[a],
M. V. Lototskyy[a, c], and B. P. Tarasov[a]

[a] *Federal Research Center of Problems of Chemical Physics and Medicinal Chemistry, Russian Academy of Sciences, Chernogolovka, Moscow oblast, 142432 Russia*

[b] *Moscow Aviation Institute (National Research University), Moscow, 125993 Russia*

[c] *University of the Western Cape, HySA Systems Centre of Competence, Robert Sobukwe Road, X17, Belville, 7535 South Africa*

*e-mail: Roz_Baz@mail.ru

**e-mail: dzhardim@icp.ac.ru; Roz_Baz@mail.ru

Abstract—In this work, Pd-doped UiO-66 metal–organic framework (MOF) was tested as a catalyst for the hydrogen absorption/desorption process. The composition, structure, and physicochemical properties of Pd-doped UiO-66 were studied using elemental analysis, IR spectroscopy, TEM, thermogravimetric and X-ray diffraction analysis. The specific surface area and pore size distribution were estimated using low-temperature nitrogen adsorption. It was shown that hydrogenation results in the formation of β-MgH_2 phase with a tetragonal crystal structure of rutile type, and the rate of the hydrogenation/dehydrogenation reaction increases in several times compared to that of Mg without additives.

THEORETICAL ANALYSIS

The problem of efficient and safe storage and transportation of hydrogen is holding back the widespread use of hydrogen energy [1, 2]. There are three main ways to store hydrogen: as a compressed gas in high-pressure tanks, in liquid form using cryogenic systems, and as a metal hydride storage method [3]. The method of storing hydrogen in metal hydrides is considered as the safest and ensures the achievement of high volumetric and gravimetric storage density [4–6].

Magnesium, as one of the most common elements in the earth's crust (2.35% by weight), and also having a high theoretical hydrogen storage capacity (7.6% by weight), is considered a promising basis for the creation of hydrogen storage materials [7]. Magnesium hydride (MgH_2) can also be used as a feedstock for hydrolysis-type hydrogen generators, in which hydrogen will be released as a result of the reaction between water (H_2O) and MgH_2 [8]. However, as studies show, pure magnesium as a hydrogen storage material exhibits poor kinetics of hydrogen absorption/desorption due to (1) presence of oxide film on its surface, (2) the slow rate of hydrogen diffusion in MgH_2/Mg, (3) the high thermodynamic stability of the Mg–H bond [7, 9]. Ball milling of Mg or MgH_2 can solve the problems of hydrogen diffusion, thereby improving the hydrogen absorption/desorption properties [9]. At the same time, the use of mechanical activation by means of the ball milling often leads to defects in the Mg structure, which become the driving force of the agglomeration processes of nanocrystalline Mg, in addition, in the absorption/desorption cycles, the material in the ball mill interacts with residual oxygen, forming layers of MgO [7].

The kinetics of hydrogen absorption/desorption can be improved and the process temperature can be reduced by adding catalysts or alloying Mg with other elements (V, Co, Zr, Ti, Nb, Mo, Ni, etc.) [10–13]. Most often, transition metal halides, rare earth metals, multivalent transition metal oxides and carbon materials are proposed as catalysts [14]. Despite numerous studies, to date there is no effective catalyst that could significantly reduce the hydrogen desorption temperature, increase the hydrogen absorption/desorption rate, or improve the cyclic stability of the hydrogen absorption/desorption process while maintaining the high hydrogen storage capacity [7]. Recently, materials prepared from metal-organic frameworks (MOFs) have been proposed as catalysts for Mg hydrogenation/dehydrogenation [15, 16].

MOFs reprsent a porous subclass of coordination networks whose structure consists of metal ions or clusters linked together by organic ligands, that have been termed as linkers [17]. Some representatives of this class of compounds are arranged in a highly ordered structure with high specific surface areas [18, 19]. The ability to adjust the size and shape of the channels of the porous structure, chemical stability and affinity for certain types of molecules provide prospects for wide practical application, including the separation and storage of gases [20–22], the separation and fine purification of substances [23, 24], in the creation of sensor materials [25–28], and for catalytic purposes [29–33]. Work in the field of application of MOFs as heterogeneous catalysts has already shown very encouraging results, in particular for direct methane oxidation processes [34], in cyanosilylation reactions, oxidation, aldol condensation and transesterification [35]. Most often, MOFs are used as catalysts with active sites on inorganic secondary block units (SBUs) of the coordination polymer or as a catalytic support functionalized with molecular catalytic complexes or nanoparticles of other transition metals [36–38]. Combining several metals in a structure often results in non-additive increases in activity or, in other words, synergistic effects [39].

In this work, Pd-doped UiO-66 was tested as a catalyst for the process of hydrogenation of magnesium and dehydrogenation of magnesium hydride. UiO-66 is a MOF consisting of $Zr_6O_4(OH)_4$ clusters connected with terephthalate linkers, known for its high chemical and thermal stability and exceptional resistance to high external pressure [40, 41]. The use of high-boiling polar solvents in the synthesis, such as DMF, and acid modulators (HCl, HBr) creates problems of environmental safety of the synthesis of UiO-66 [40, 41]. Previously, we proposed a fast and environmentally friendly approach to the preparation of highly porous UiO-66 ($S_{BET} \approx 900$ m²/g), and also demonstrated excellent stability in the hydrogenation reaction of unsaturated compounds by Pd-doped UiO-66 [42, 43]. In this paper, we demonstrate the potential possibility of using Pd-doped UiO-66 as a catalyst for the hydrogen absorption in magnesium and hydrogen desorption from its hydride, MgH_2.

EXPERIMENTAL

Reagents

Zirconyl chloride octahydrate ($ZrOCl_2 \cdot 8H_2O$, p.a.), terephthalic acid ($C_8H_6O_4$, BDC, p.a.), Potassium chloride (KCl, ch.pr.), palladium (II) chloride ($PdCl_2$, ch.pr.), acetic acid (CH_3COOH, p.a) and potassium hydroxide (KOH, p.a.) were purchased from Ruskhim chemical company (Moscow, Russia) and were used without further purification. Polyethylene Glycol 1500 (PEG-1500 for synthesis), magnesium hydride (powder, hydrogen storage grade) and methanol (ACS reagent, ≥99.8%) were supplied by Sigma-Aldrich company.

Preparation of Pd/ UIO-66 Catalyst

UiO-66 was synthesized using a previously developed technique [42]. 18 mL of 2 M CH_3COOH were added dropwise to 18 mL of 1 M $ZrOCl_2 \cdot 8H_2O$ to obtain a hexanuclear zirconium cluster. The resulting mixture was kept at 55°C for 120 min. Terephthalic acid (3.00 g; 0.0180 mol) dissolved in 100 mL an aqueous KOH solution (2.02 g; 0.036 mol) was added to the hexanuclear zirconium cluster solution. The mixture was left stirring for 120 min at room temperature. The resultant white solid precipitate (UiO-66) was isolated by filtration and washed several times with distilled water. The preparation of Pd/UiO-66 was carried out in the manner described by us earlier [43]. Resulting Pd/UiO-66 was treated with methanol in a Soxhlet extractor (16 h, 70°C) and dried in vacuum (10^{-3} Torr, 80°C, 2 h) to remove the solvent physically adsorbed in the pores. According to the results of elemental analysis, the final product (yield: 5.8 g, 98%) contained 31.4, 2.8 and 1.8 ± 0.1 wt % C, H and Pd, respectively.

Characterization Methods

ATR-FTIR spectra were recorded using infrared spectrometer (Bruker Alpha, USA) with a diamond prism of single reflection in the range of 360–4000 cm⁻¹ at room temperature using 24 scans and a resolution of 2 cm⁻¹. The penetration depth for a medium with a sufficiently deep refractive index (2.43) at 1000 cm⁻¹ is 1.66 microns. The baseline of the obtained spectra was corrected in the OPUS program. The specific surface, pore volume and pore diameter of samples were measured on Autosorb-1 automatic analyzer (Quantachrome, USA). The specific surface was calculated by the BET method and the pore volume and pore diameter of samples were calculated by DFT method. The phase analysis was performed on an Aeris Benchtop powder diffractometer (Malvern PANalytical, the Netherlands) using Cu-Kα radiation ($\lambda = 1.5406$ Å, scanning step 0.012°, measurement range $2\theta = 5°–90°$). The Pd content was analyzed by inductively coupled plasma the atomic absorption spectrometer "AAS-3" (Zeiss, Germany). The thermal stability of Pd/UiO-66 was evaluated using a TGA/SDTA851e Mettler Toledo thermal analyzer (Mettler Toledo, Switzerland). The sample was heated in a nitrogen atmosphere at a heating rate of 10°C/min at a temperature range from 25 to 600°C. The contents of carbon (C), hydrogen (H), nitrogen (N) were determined using elemental analyzer (MICRO Cube, Germany). The morphology and distribution of palladium nanoparticles were studied using a JEOL JEM-2100 PLUS universal transmission electron microscope (JEOL, Japan) with an accelerating voltage of 200 kV.

The sample was dispersed in isopropyl alcohol using ultrasound. The resulting solution was dropped onto a copper grid coated with an amorphous carbon film. INCA ENERGY analytical system attachment to the TEM (Oxford Instruments, USA) was used for Energy dispersive x-ray microanalysis.

Catalytic Activity Test

Commercial magnesium hydride (MgH_2) powder was used as the starting material. The as-delivered MgH_2, or its mixture with Pd/UIO-66 catalyst (1, 5, and 10 wt % as respect to MgH_2; total weight 0.5 g) was ball milled in a Fritsch Pulverisette 6 planetary mill under hydrogen atmosphere ($P = 0.5$ MPa), at the disc rotation speed of 300 rpm, for 1 h. The ball to powder weight ratio was 160/1. The ball milled sample was reloaded from the milling vial to hydrogenation/dehydrogenation reactor in a glovebox (MBraun) under the atmosphere of purified argon (water and oxygen content no more than 0.0001%). The reactor was connected to an in-house made volumetric Sieverts setup followed by the hydrogen absorption/desorption experiments carried out in the following sequence:

(a) Evacuating the reactor.

(b) Hydrogen desorption at $T = 350°C$ and the starting H_2 pressure $P(H_2) = 0.11$ MPa.

(c) Hydrogen absorption at $T = 300°C$ and the starting H_2 pressure $P(H_2) = 0.56$ MPa.

The pressure changes in the system when carrying out H_2 desorption (b) and H_2 absorption (c) experiments did not exceed 0.01 MPa that allows to consider kinetics of both processes as isobaric.

The procedures (b) and (c) were repeated three times when the first and the second H_2 desorption/absorption cycles were performed for the sample activation, and kinetic data of the H_2 desorption/absorption were collected at the third cycle. The number of moles, $\Delta n(t)$, of the desorbed (b) or absorbed (a) hydrogen at the moment t was determined as the absolute value of the difference between the starting, n_0, and the actual, $n(t)$, numbers of moles of hydrogen in the reactor and the volumetric system:

$$\Delta n(t) = |n_0 - n(t)|; \qquad (1)$$

$$n_0 = \frac{P_0(s)V(s)}{Z_1 RT(s)} + \frac{P_0(r)V(r)}{Z_2 RT(r)}; \qquad (2)$$

$$n(t) = P(t)\left[\frac{V(s)}{Z_1 RT(s)} + \frac{V(r)}{Z_2 RT(r)}\right]; \qquad (3)$$

where $P_0(s)$ and $P_0(r)$ are the starting H_2 pressures in the volumetric system and the reactor of volumes $V(s)$ and $V(r)$ kept at the temperatures $T(s)$ and $T(r)$, respectively; $P(t)$ is the actual hydrogen pressure; R is the universal gas constant; Z_1 and Z_2 are the hydrogen compressibility factors at the temperatures and pressures in the volumetric system and the reactor, respectively. Due to the low hydrogen pressures during the experiments (0.1–0.6 MPa), both Z_1 and Z_2 were assumed to be equal to one.

From the measured values of $\Delta n(t)$, the reacted fraction, $\alpha(t)$ was calculated as:

$$\alpha(t) = \frac{\Delta n(t)}{\Delta n_{max}}; \qquad (4)$$

where Δn_{max} is the maximum theoretical number of moles H_2 which corresponds to the full transformation of Mg in the sample to MgH_2 (absorption) or MgH_2 to Mg (desorption).

Formal kinetic analysis of the collected $\alpha(t)$ data was carried out by their fitting with the Avrami–Erofeev equation in the form [44]:

$$\alpha(t) = \alpha_{max}\left\{1 - \exp\left[-(t/t_0)^n\right]\right\}; \qquad (4)$$

where $\alpha_{max} \leq 1$ is the maximum (asymptotic) value of the reacted fraction; t_0 is the characteristic reaction time (reciprocal rate constant, $t_0 = 1/k$) equal to the time required to achieve $(1 - 1/e) \approx 63\%$ transformation; and n is the Avrami exponent related to the reaction mechanism.

RESULTS AND DISCUSSION

Physicochemical Properties of the Catalyst Pd/UIO-66

Solvothermal synthesis is the most used method for obtaining UiO-66 [41, 45, 46], involving the use of inorganic metal salts as a precursor to an inorganic block and heating a mixture of an organic linker and a metal salt in a system of high-boiling polar solvents such as DMFA. The disadvantages of this synthesis include high reaction temperatures, as well as uncontrolled formation of inorganic components directly during the reaction, which often results in the formation of mixed phases of MOFs [47]. In this regard, attempts to synthesize chemically stable metalorganic frameworks based on polynuclear inorganic clusters prove to be a very difficult task. In this work, rational approach in the preparation of MOFs, which suggests the use of polynuclear molecular complexes as a source of secondary building units (SBUs), was used to obtain UiO-66 [48, 49]. Previously, we selected the optimal conditions for obtaining highly porous UiO-66 using aqueous solutions of the $[Zr_6O_4(OH)_4(CH_3COO)_{12}]$ complex [43].

The phase composition and purity of the resulting Pd/UIO-66 were confirmed by elemental analysis, IR spectroscopy (Fig. 1) and XRD analysis (Fig. 3).

Main characteristic peaks in the IR spectrum of Pd/UiO-66 shows very good agreement with the literature data [50, 51]. According to the ATR spectrum of Pd/UiO-66 (Fig. 1), an intense and broad absorption band centered at 3150 cm^{-1} can be attributed to the
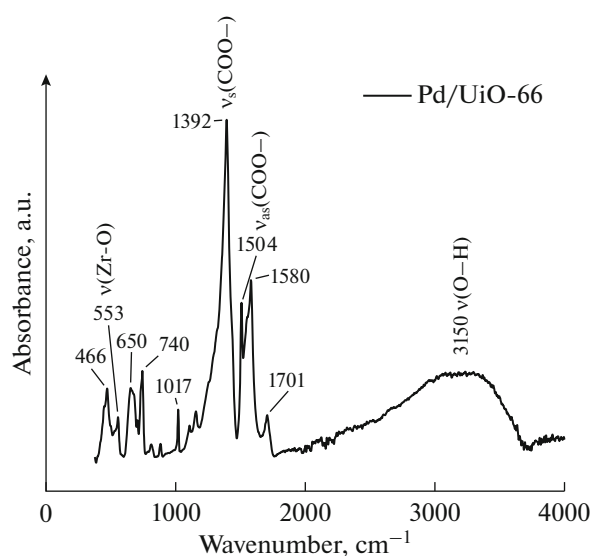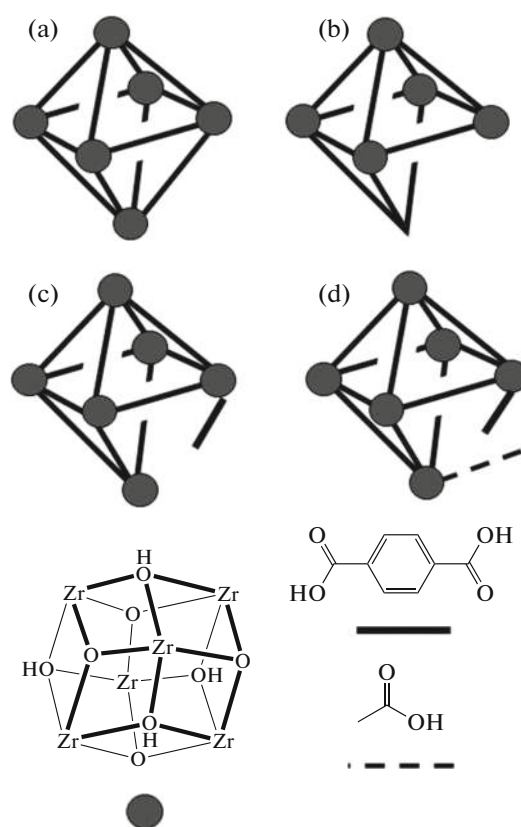
Fig. 1. ATR-FTIR spectrum of Pd/UiO-66.

Fig. 2. Schematic representation of linker defects in an octahedral pore of UiO-66; (a) defect-free structure; (b) missing linker; (c) dangling linker; (d) dangling modulator.

stretching vibrations of the −OH group of crystallization water condensed inside the cavities of the MOF [52]. The stretching vibrations ν(C−H) of the benzene ring are very weakly manifested in the range of 2950−2750 cm^{-1} due to the low sensitivity of the ATR spectrum. Asymmetric stretching vibrations of the carboxyl group ν_{as}(COO$^-$) are manifested in the region of 1620−1550 cm^{-1} with a maximum intensity at 1580 cm^{-1}, symmetric stretching vibrations of the carboxyl group ν_s(COO$^-$) are appeared in the region of 1415−1380 cm^{-1} with a maximum at 1392 cm^{-1} ($\Delta = \nu_{as}$(COO$^-$)−ν_s(COO$^-$) = 180−190 cm^{-1}). The IR spectrum contains a weak absorption band in the region of 1694−1710 cm^{-1}, which can be attributed to the stretching vibrations ν(C=O) in aromatic acids. The appearance of such a band can be explained by the presence of dangling-linker defects in the resulting structure, as well as by the possibility of incomplete replacement of the acetic acid modulator, leading to the presence of dangling modulators [53]. In this case, the BDC linker does not link two inorganic SBUs of MOF, but attaches to only one, "dangling" between the links, leaving the inorganic unit coordinatively unsaturated. A schematic representation of possible defects in the structure is shown in Fig. 2. We have previously shown that the reaction duration, pH of the medium, and the amount of modulator play a decisive role in the implementation of the complete replacement of acetate residues with terephthalate ones in achieving high surface area and thermal stability values of the target UiO-66 [43].

The vibration band with the absorption maximum at 1504 cm^{-1} is attributed to the stretching vibrations of the C=C benzene ring [50]. Plane deformation vibrations δ(C−H) of the benzene ring are detected at

1017 cm^{-1}. A weak peak at 768 cm^{-1} corresponds to out-of-plane deformation vibration =C−H in substituted benzene derivatives [52]. Stretching vibrations of the Zr−O−C bond appeared at lower frequencies (650 and 553 cm^{-1}). The peak at 466 cm^{-1} is attributed to the bending mode (HO)−Zr−(OH) [50].

The position of the narrow diffraction maxima (Fig. 3) confirms the proposed crystal structure, thus UiO-66 crystallizes in $Fm\bar{3}m$ space group with an experimental lattice parameter (a = 20.768 Å) [54]. The most intense Bragg reflections with centers at 7.36°, 8.50° and 25.73° correspond to the reflection planes (111), (200) and (600) of the crystal lattice, respectively [55]. A broadening of the most intense peak is observed, which can be explained by the presence of defects in the structure, the formation of which, as mentioned earlier, can be due to the competition of acetic acid for carboxylate sites on $Zr_6O_4(OH)_4(CO_2)_{12}$ clusters with terephthalic acid [56]. The diffraction peaks at 40.12°, 46.81° and 82.1° correspond to the face-centered cubic (FCC) structure of the Pd(0) phase according to JCPDS No. 46-1043. It should be noted that the reduction of Pd(II) to Pd(0) does not affect the XRD profile of UiO-66.
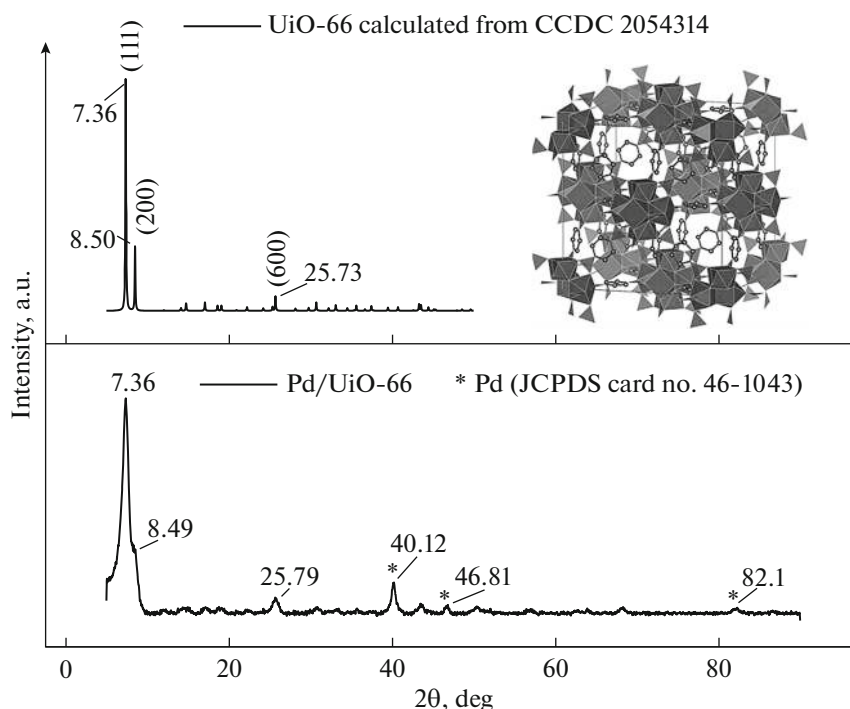
Fig. 3. Diffraction pattern of Pd/UiO-66 compared to the calculated.

TEM micrographs were used for microanalysis, construction of particle size distribution histograms and calculation of their average diameter (Fig. 4). Palladium nanoparticles are spherical and uniformly distributed over the UiO-66 surface. The average particle size ranged from 8 to 12 nm. The energy-dispersive spectrum (Fig. 4c) contains signals of Zr, C and O atoms contributed by both the BDC linker and the inorganic unit. X-ray emission from Pd nanoparticles is also recorded. Copper signals appear from the copper substrate on which the studied sample was deposited.

The possibility of using MOFs in magnesium hydrogenation largely depends on the temperature limits of their thermal stability. It is known that thermal degradation of MOFs in most cases is the result of the destruction of the metal/cluster—ligand bond accompanied by or following the combustion of the linker [57]. Consequently, thermal stability is usually related to the strength of the metal/cluster—ligand bond. The use of symmetrical linkers with higher valence metal centers, such as Ln(III), Al(III), Zr(IV), and Ti(IV), improves the thermal stability of MOFs by increasing the strength of the metal—ligand bond [58, 59]. Thermal stability can also be improved by changing the composition and length of the linker. As a rule, the linker should be short and should not contain functional groups capable of coordinating the metal, at least in the immediate vicinity of the metal nodes [60]. UiO-66 consisting of high-valent inorganic Zr^{4+} units and BDC linkers demonstrates excep-

tionally high thermal and chemical stability [51]. According to the TGA and dTGA curves, the introduction of palladium nanoparticles (2 wt %) into the UiO-66 structure does not affect the thermal stability of the final material. Pd/UiO-66 exhibits three main decomposition stages. The first decomposition stage occurs up to 175°C with a weight loss of up to 6.65 wt % and is associated with the loss of physically absorbed solvent molecules. The second decomposition stage occurs in the range from 175 to 380°C with a weight loss of about 11.77 wt % and can be attributed to the elimination of coordinated solvent molecules/solvent molecules located in the pores. Such a high temperature of molecule elimination indicates strong coordination interactions between the coordination center (Zr(IV)) and solvent molecules, which is in good agreement with the data previously described by a number of other researchers for UiO-66 obtained by other methods [50, 61, 62]. The third stage of decomposition with the maximum decomposition rate at 550°C is associated with the combustion of the terephthalic acid linker (−35.44 wt %) and is accompanied by the formation of zirconium (IV) oxide. Previously, Valenzano L. et al. showed that TGA can be used to detect defects in the structure of UiO-66 [50]. It is very likely that during combustion of Pd/UiO-66 the final residue (46.14% by weight) at high temperature (600°C) is ZrO_2 with a small content of palladium oxide (up to 2.2% by weight). It is easy to calculate that with a mass loss of up to 36% in the third stage, about 5 of the 6 necessary linkers are lost per inorganic clus-
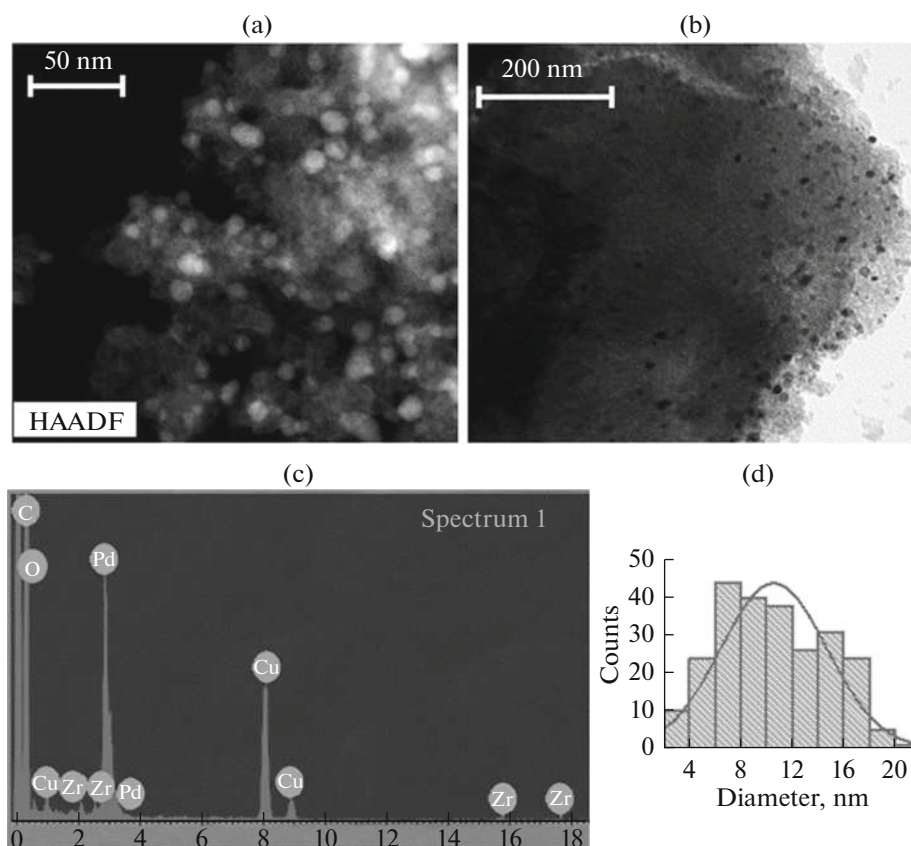
Fig. 4. (a) HAADF-STEM, (b) TEM image and (c) EDX spectrum of Pd/UiO-66; (d) distribution of palladium nanoparticles.

ter $Zr_6O_4(OH)_4$. This means that the synthesized material has small missing linker defects that arise randomly and are difficult to detect by crystallographic methods [50]. The presence of defects in the UiO-66 structure, as a rule, increases the catalytic activity of

the material, since the formation of coordinatively unsaturated sites of Zr^{4+}, as well as hydrolyzed $(HO)-Zr-(OH)$ allows us to consider inorganic nodes as Lewis/Brønsted centers [63, 64].
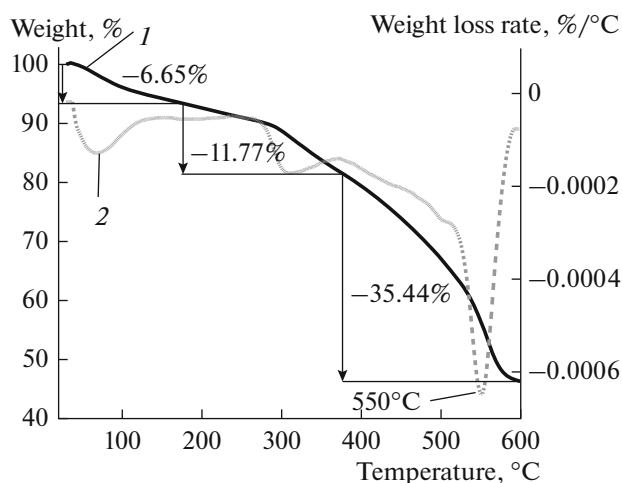
The specific surface characteristics were estimated using low-temperature nitrogen adsorption (Fig. 6). According to the obtained data, the introduction of Pd nanoparticles into UiO-66 reduces S_{BET} from 890 to 476 m^2/g and decreases the pore volume V_{BJH} from 0.78 to 0.72 cm^3/g. A similar decrease in the specific surface area and pore volume was observed upon the introduction of platinum Pt(0) and palladium Pd(0) nanoparticles into MIL-101 [65, 66]. The authors attribute the noticeable decrease in the amount of sorbed N_2 and the decrease in pore volume to the high concentration of dispersed nanoparticles in the framework cavity or/and blocking of surface-located NPs from accessing the surface. The obtained adsorption isotherms correspond to type IV adsorption isotherms according to the IUPAC classification, indicating the occurrence of polymolecular adsorption in mesoporous systems with irreversible capillary condensation (hysteresis). The observed hysteresis loops are characteristic of materials with a slit-shaped pore shape [67].
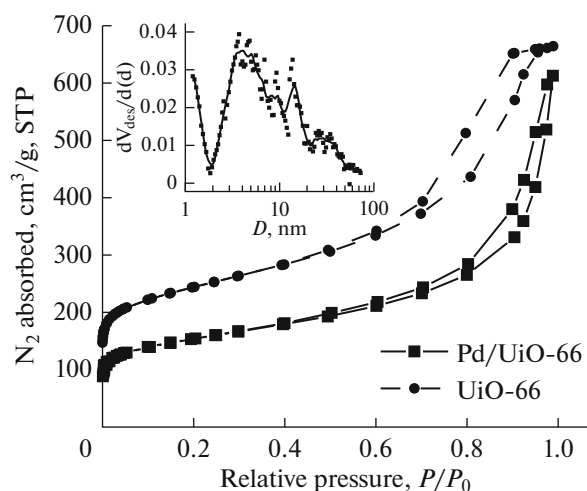

Fig. 5. TGA (*1*) and dTGA (*2*) profiles of Pd/UiO-66 performed under a nitrogen atmosphere at a heating rate of 10°C/min.

Fig. 6. Nitrogen adsorption-desorption isotherm and differential pore diameter distribution calculated by DFT method for a Pd/UiO-66.

Fig. 7. Observed (symbols) and calculated (lines) time dependencies of reacted "Mg–MgH$_2$" fraction during hydrogenation at $T = 300°C$, $P = 0.56$ MPa of the samples without (*1*) and with 1 (*2*), 5 (*3*) and 10 wt % (*4*) of the Pd/UiO-66 catalyst.

The results of catalytic activity test in the magnesium hydrogenation/dehydrogenation are shown in Figs. 7–8. Experimental results show that magnesium hydrogenation in the presence of 10 wt % Pd/UiO-66 (about 0.18 wt % of Pd metal) allows achieving 82% conversion already after 3 minutes of the process. β-MgH$_2$ phase with a tetragonal crystal structure of rutile type was formed (JCPDS card No. 12-697) according to the results of the X-ray analysis (Fig. 9). Moreover, there are no peaks of unreacted Mg in the diffraction patterns when using 5–10 wt % of the catalyst additive. The IR spectra of the reaction products showed two broad absorptions with maxima at 1144, 642 and 533 cm^{-1}, which is in good agreement with the published IR spectra of solid magnesium dihydride [68]. A correlation between the degree of Mg conversion into MgH$_2$ and the intensity of signals in the ATR-FTIR spectra is observed. The peaks corresponding to Pd/UiO-66 are absent in the reaction products that can be explained by destruction of the MOF structure under the harsh ball milling conditions. At the same time, it is clear that introducing Pd/UiO-66 catalyst (≤0.18 wt % as respect to Pd metal) results in the significant improvements of both hydrogenation (Fig. 7) and dehydrogenation (Fig. 8) kinetics. This observation is in contrast with the results of the study of Mg(MgH$_2$)–Pd ball-milled composites when introducing palladium as 0.1 wt % of Pd black did not result in the improvement of hydrogen sorption performance [69]. Therefore, independently on the possible changes of the UiO-66 MOF structure during preparation of the Mg(MgH$_2$)–Pd/UiO-66 composites, the former can be considered as a very effective precursor of introducing minor amounts of catalytic Pd nanoparticles into the composite.
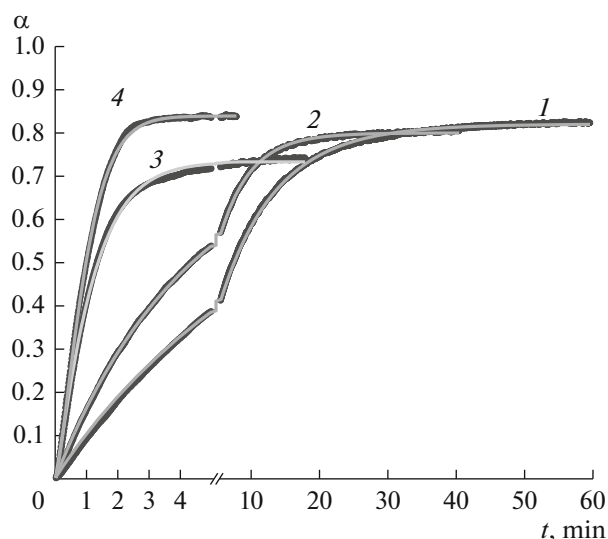
Tables 1–2 summarize the values of kinetic parameters of hydrogen absorption and desorption, respectively, obtained by the fitting of the experimental data (Figs. 7–8) with Eq. (4). The presented refined kinetic parameters (α_{max}, t_0, n) are supplemented by the values of their refining errors which correspond to the last decimal digit presented in the brackets. The corre-
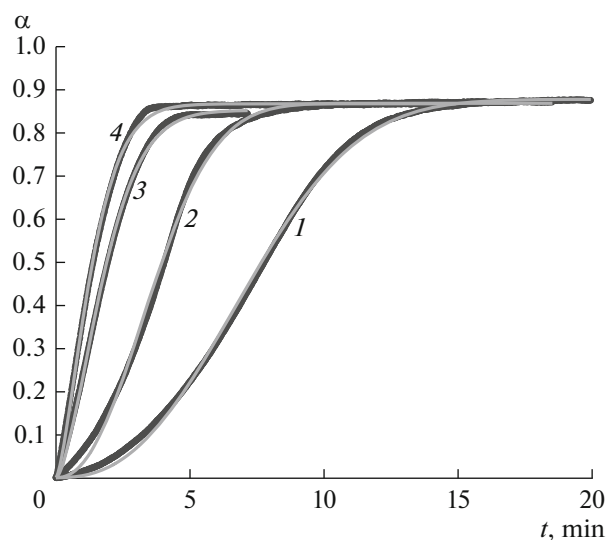

Fig. 8. Observed (symbols) and calculated (lines) time dependencies of reacted "MgH$_2$–Mg" fraction during dehydrogenation at $T = 350°C$, $P = 0.11$ MPa of the samples without (*1*) and with 1 (*2*), 5 (*3*) and 10 wt % (*4*) of the Pd/UiO-66 catalyst.
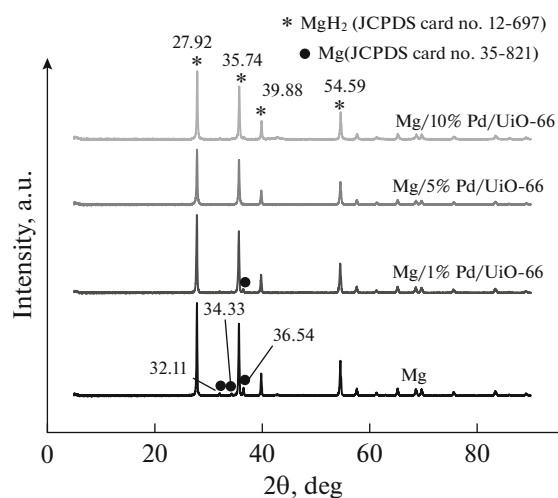
Fig. 9. Diffraction patterns of magnesium hydrides obtained without a catalyst (Mg) and the addition of various amounts of Pd/UiO-66.
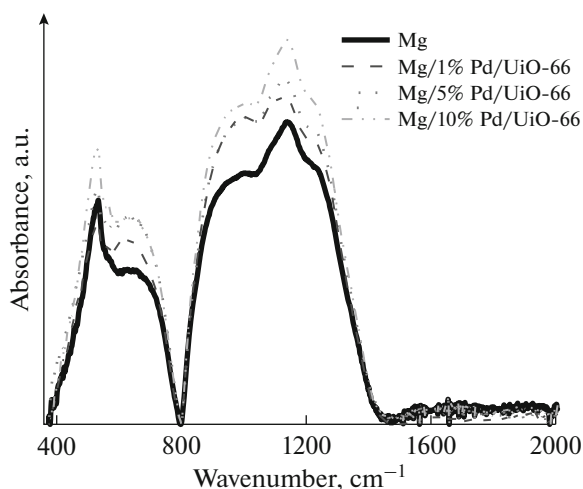

Fig. 10. ATR-FTIR spectra of magnesium hydrides obtained without a catalyst (Mg) and the addition of various amounts of Pd/UiO-66.

sponding values of the rate constants, $k = 1/t_0$, are presented as well.

It can be seen from Tables 1–2 that in all the cases the fitting was very good corresponding to the Pearson correlation coefficient, R^2, above 0.998, also confirmed by almost complete coincidence of the experimental data points and calculated curves (Figs. 7–8).

The values of n for the H_2 absorption (Table 1) in most cases are close to 1 associated with grain boundary nucleation mechanism [44] and/or contribution of H diffusion in the solid [70]; the increase of Pd/UiO-66 content in the composite results in a gradual increase of n to ~1.34 for Mg + 10 wt % Pd/UiO-66 testifying about contribution of the nucleation and growth in the bulk material. The increase of Pd/UiO-66 content results in the gradual decrease of n for the H_2 desorption from ~2.5 for the unmodified MgH_2 (nucleation and growth) to ~1.45 for MgH_2 + 10 wt % Pd/UiO-66 that testifies about growing contribution of the surface (grain boundary) processes into overall reaction.

Figure 11 presents dependencies of the calculated rate constants on the amount of the additive of Pd/UiO-66 catalyst (squares) into Mg-based hydrogen storage composite. It is seen that the increase of the amount of the catalyst results in a significant improvement of both H_2 absorption and H_2 desorption kinetics. For the composite containing 10 wt % Pd/UiO-66, the H_2 absorption and desorption rate constants increase in 7.6 and 5.2 times, respectively. The improvements are similar to the ones observed for the Mg-based composites with graphene-like material modified with nickel nanoparticles (Ni/GLM) at similar H_2 absorption/desorption conditions [44]—the corresponding data are shown in Fig. 11 as diamonds. The use of Pd/UiO-66 catalyst is especially efficient for the accelerating of H_2 desorption process; the improvements are 1.65 times higher than in the case of use of Ni/GLM catalyst. Obviously, the acceleration of the rate of hydrogen absorption/desorption is associated with the use of nanoscale palladium characterized by a strong catalytic effect in the processes of dissociative chemisorption of H_2 molecules (H_2 absorption) and recombination of H atoms (H_2 desorption) on the surface of Mg/MgH$_2$.

Table 1. Kinetic parameters of hydrogen absorption in the studied samples

Sample	Kinetic parameters				R^2
	α_{max}	t_0, min	k, min^{-1}	n	
Mg	0.8226(1)	8.025(5)	0.1246	0.967(1)	0.9993
Mg + 1 wt % Pd/UiO-66	0.8020(1)	4.475(3)	0.2235	0.985(1)	0.9997
Mg + 5 wt % Pd/UiO-66	0.7348(2)	1.210(3)	0.8264	1.131(4)	0.9971
Mg + 10 wt % Pd/UiO-66	0.8414(2)	1.051(1)	0.9515	1.339(3)	0.9995

Table 2. Kinetic parameters of hydrogen desorption from the studied samples

Sample	Kinetic parameters				R^2
	α_{max}	t_0, min	k, min^{-1}	n	
MgH$_2$	0.8794(3)	8.229(5)	0.1215	2.494(5)	0.9995
MgH$_2$ + 1 wt % Pd/UiO-66	0.8702(3)	4.241(4)	0.2358	2.236(6)	0.9984
MgH$_2$ + 5 wt % Pd/UiO-66	0.8537(8)	2.055(4)	0.4866	1.584(6)	0.9990
MgH$_2$ + 10 wt % Pd/UiO-66	0.8688(3)	1.517(3)	0.6592	1.455(6)	0.9990

CONCLUSIONS

In this work, UIO-66 was prepared using a rational method for synthesizing MOFs using a hexanuclear Zr(IV) oxo-acetate cluster as SBU. Using this method of synthesis allows the target structure to be obtained quickly and with a high reaction yield but leads to the appearance of minor defects.

Post-synthetic modification of UIO-66 was carried out by introducing catalytically active Pd nanoparticles (1.8 wt %). According to the obtained data, the introduction of Pd nanoparticles into UiO-66 reduces SBET from 890 to 476 m^2/g and decreases the pore volume V_{BJH} from 0.78 to 0.72 cm^3/g but does not affect the thermal stability and structure.

The principal opportunity of using Pd-doped UiO-66 as an effective catalyst for the process of hydrogenation of magnesium and dehydrogenation of magnesium hydride was demonstrated.
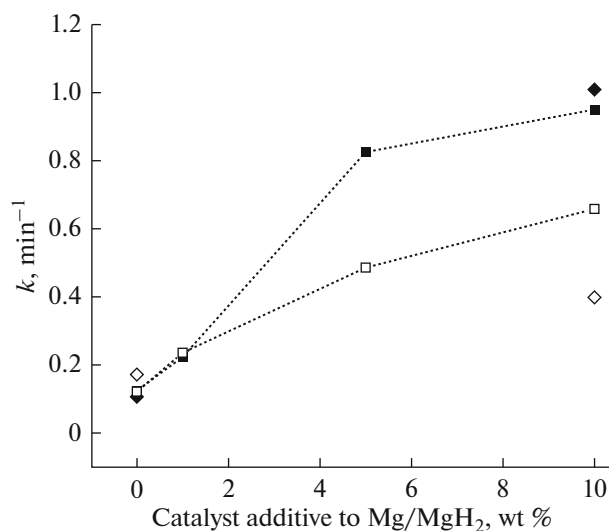

Fig. 11. Rate constants of H$_2$ absorption (filled symbols) and H$_2$ desorption (empty symbols) depending on the percentage of catalyst additive to Mg (MgH$_2$). Squares—Pd/UiO-66 (this work), diamonds—Ni/GLM [44].

CONFLICT OF INTEREST

The authors of this work declare that they have no conflicts of interest.

REFERENCES

1. Yang, M. et al., *Clean Energy*, 2023, vol. 7, no. 1, p. 190.
2. Manoharan, Y. et al., *Appl. Sci.*, 2019, vol. 9, no. 11, p. 2296.
3. Uesugi, H. et al., J. Jpn. Inst. Light Met., 2010, vol. 60, no. 11, p. 615.
4. Bellosta von Colbe, J. et al., *Int. J. Hydrogen Energy*, 2019, vol. 44, no. 15, p. 7780.
5. Yartys, V.A. et al., *Int. J. Hydrogen Energy*, 2019, vol. 44, no. 15, p. 7809.
6. Tarasov, B.P. et al., *Russ. J. Phys. Chem*. A, 2020, vol. 94, no. 5, p. 996.
7. Lyu, J., Lider, A., and Kudiiarov, V., *Metals*, 2019, vol. 9, no. 7, p. 768.
8. Tarasov, B.P., *Int. J. Hydrogen Energy*, 2011, vol. 36, no. 1, p. 1196.
9. Xie, X. et al., *Int. J. Hydrogen Energy*, 2019, vol. 44, no. 21, p. 10694.
10. Luo, Q. et al., *J. Magnesium Alloys*, 2019, vol. 7, no. 1, p. 58.
11. Yang, T. et al., *Energy*, 2018, vol. 165, p. 709.
12. Li, Q. et al., *Int. J. Hydrogen Energy*, 2004, vol. 29, no. 8, p. 843.
13. Wu, C. et al., *J. Phys. Chem*. B, 2005, vol. 109, no. 47, p. 22217.
14. Yang, Y. et al., *J. Mater. Sci. Technol.*, 2023, vol. 163, p. 182.
15. Shao, H. et al., *Int. J. Hydrogen Energy*, 2021, vol. 46, no. 76, p. 37977.
16. Huang, T. et al., *Chem. Eng. J.*, 2021, vol. 421, p. 127851.
17. Batten, S.R. et al., *Pure Appl. Chem.*, 2013, vol. 85, no. 8, p. 1715.

18. Farha, O.K. et al., *J. Am. Chem. Soc.*, 2012, vol. 134, no. 36, p. 15016.

19. Al-Othman, A. et al., *Reference Module in Materials Science and Materials Engineering*, Hashmi, M.S.J., Ed., Elsevier, 2020.

20. Jia, T., Gu, Y., and Li, F., *J. Environ. Chem. Eng.*, 2022, vol. 10, no. 5, p. 108300.

21. Li, H. et al., *Energy Chem.*, 2019, vol. 1, no. 1, p. 100006.

22. Li, H. et al., *Mater. Today*, 2018, vol. 21, no. 2, p. 108.

23. Hu, Y. et al., *Chem. Commun.*, 2010, vol. 47, p. 737.

24. Dybtsev, D.N. et al., *Inorg. Chem.*, 2007, vol. 46, no. 17, p. 6843.

25. Gonçalves, J.M. et al., *J. Mater. Chem*. C, 2021, vol. 9, no. 28, p. 8718.

26. Zuliani, A., Khiar, N., and Carrillo-Carrion, C., *Anal. Bioanal. Chem.*, 2023, vol. 415, no. 11, p. 2005.

27. Yi, F.-Y., Chen, D., Wu, M.-K., Han, L., and Jiang, H.-L., *ChemPlusChem*, 2016, vol. 81, no. 8. p. 675.

28. Shukla, A.K. et al., *J. Inorg. Organomet. Polym. Mater.*, 2024, vol. 34, no. 8, p. 3457.

29. Jaryal, R., Kumar, R., and Khullar, S., *Coord. Chem. Rev.*, 2022, vol. 464, p. 214542.

30. Deria, P. et al., *J. Am. Chem. Soc.*, 2016, vol. 138, no. 43, p. 14449.

31. Zhang, Y. et al., *Chem. Eng. J.*, 2019, vol. 369, p. 745.

32. Gong, Y. et al., *J. Catal.*, 2020, vol. 392, p. 141.

33. Bondarenko, L. et al., *New J. Chem.*, 2024, vol. 48, p. 1039.
https://doi.org/10.1039/d4nj00963k

34. Baek, J. et al., *J. Am. Chem. Soc.*, 2018, vol. 140, no. 51, p. 18208.

35. Dhakshinamoorthy, A., Alvaro, M., and Garcia, H., *Chem. Commun.*, 2012, vol. 48, no. 92, p. 11275.

36. Gupta, V. and Mandal, S.K., *Inorg. Chem.*, 2020, vol. 59, no. 7, p. 4273.

37. Pascanu, V. et al., *J. Am. Chem. Soc.*, 2019, vol. 141, no. 18, p. 7223.

38. Qin, J.-S. et al., *Chem. Commun.*, 2018, vol. 54, no. 34, p. 4231.

39. Huang, Y.-B. et al., *Chem. Soc. Rev.*, 2017, vol. 46, no. 1, p. 126.

40. Ahmadijokani, F. et al., *Prog. Mater. Sci.*, 2022, vol. 125, p. 100904.

41. Zou, D. and Liu, D., *Mater. Today: Chem.*, 2019, vol. 12, p. 139.

42. Baimuratova, R.K. et al., *J. Compos. Sci.*, 2022, vol. 6, no. 10, p. 299.

43. Andreeva, A.V. et al., *Eurasian J. Chem.*, 2024, p. 31489.
https://doi.org/10.31489/2959-0663/3-24-10

44. Tarasov, B.P., Arbuzov, A.A., Mozhzhukhin, S.A., et al., *Int. J. Hydrogen Energy*, 2019, vol. 44, p. 29212.

45. Bae, S., et al., *Korean J. Chem. Eng.*, 2018, vol. 35, no. 3, p. 764.

46. Pourmadadi, M. et al., *J. Drug Deliv. Sci. Technol.*, 2022, vol. 76, p. 103758.

47. Huang, L., *Microporous Mesoporous Mater.*, 2003, vol. 58, no. 2, p. 105.

48. Yaghi, O.M. et al., *Nature*, 2003, vol. 423, no. 6941, p. 705.

49. Ockwig, N.W. et al., *Acc. Chem. Res.*, 2005, vol. 38, no. 3, p. 176.

50. Valenzano, L. et al., *Chem. Mater.*, 2011, vol. 23, no. 7, p. 1700.

51. Kandiah, M. et al., *Chem. Mater.*, 2010, vol. 22, no. 24, p. 6632.

52. Nakamoto, K., *Infrared and Raman spectra of Inorganic and Coordination Compounds*, Hoboken, NJ: Wiley, 2009, 6th ed.

53. Pakamorė, I. et al., *Green Chem.*, 2018, vol. 20, no. 23, p. 5292.

54. Ma, Y. et al., *J. Am. Chem. Soc.*, 2021, vol. 143, no. 29, p. 10977.

55. Yan, F. et al., *J. Mater. Sci.*, 2021, vol. 56, no. 16, p. 10008.

56. Shearer, G.C. et al., *Chem. Mater.*, 2016, vol. 28, no. 11, p. 3749.

57. Healy, C. et al., *Coord. Chem. Rev.*, 2020, vol. 419, p. 213388.

58. Kalidindi, S.B. et al., Angew. Chem., Int. Ed. Engl., 2015, vol. 54, no. 1, p. 221.

59. Devic, T. and Serre, C., *Chem. Soc. Rev.*, 2014, vol. 43, no. 16, p. 6097.

60. Makal, T.A., Wang, X., and Zhou, H.-C., *Crystal Growth Des.*, 2013, vol. 13, no. 11, p. 4760.

61. Taddei, M., van Bokhoven, J.A., and Ranocchiari, M., *Inorg. Chem.*, 2020, vol. 59, no. 11, p. 7860.

62. Vetlitsyna-Novikova, K.S. et al., *J. Surf. Invest.: X-ray, Synchrotron Neutron Tech.*, 2019, vol. 13, no. 5, p. 787.

63. Feng, X., et al., *ACS Apl. Mater. Interfaces. American Chemical Society*, 2021, vol. 13, no. 51, p. 60715.

64. Feng, Y., et al., *Ind. Eng. Chem. Res.*, 2019, vol. 58, no. 38, p. 17646.

65. Yang, Q., et al., *Chem. Commun. The Royal Society of Chemistry*, 2015, vol. 51, no. 52, p. 10419.

66. Aijaz, A., et al., *J. Am. Chem. Soc. American Chemical Society*, 2012, vol. 134, no. 34, p. 13926.

67. Schneider, P., *Aplied Catalysis A: General.*, 1995, vol. 129, no. 2. p. 157.

68. Wang, X. and Andrews, L., *The Journal of Physical Chemistry A*, 2004, vol. 108, no. 52, p. 11511.

69. Williams, M., Sibanyoni, J.M., Lototskyy, M., and Pollet, B.G., *Journal of Alloys and Compounds*, 2013, vol. 580, p. S144.

70. Rudman, P.S., *J. Apl. Phys.*, 1979, vol. 50, no. 11, p. 7195.